Multilevel plane wave time domain–based global boundary kernels for two-dimensional finite difference time domain simulations

Mingyu Lu, Meng Lv, and Arif A. Ergin

Center for Computational Electromagnetics, Department of Electrical and Computer Engineering, University of Illinois at Urbana-Champaign, Urbana, Illinois, USA

Balasubramaniam Shanker

Electromagnetics Research Group, Department of Electrical and Computer Engineering, Michigan State University, East Lansing, Michigan, USA

Eric Michielssen

Center for Computational Electromagnetics, Department of Electrical and Computer Engineering, University of Illinois at Urbana-Champaign, Urbana, Illinois, USA

Received 27 June 2003; revised 3 February 2004; accepted 1 June 2004; published 14 August 2004.

[1] Time domain boundary integrals are used to impose global transparent boundary conditions in two-dimensional finite difference time domain solvers. Augmenting classical methods for imposing these conditions with the multilevel plane wave time domain scheme reduces the computational cost of enforcing a global transparent boundary condition from $O(\tilde{N}^{s^2}\tilde{N}^{t^2})$ to $O(\tilde{N}^s\tilde{N}^t \log \tilde{N}^s \log \tilde{N}^t)$; here $\tilde{N}^s$ and $\tilde{N}^t$ denote the number of equivalent source boundary nodes and their time samples used to integrate external fields, respectively. Numerical results demonstrate that for thin and concave material objects, plane wave time domain-accelerated global transparent boundary kernels outperform perfectly matched layer-based absorbing boundary schemes without loss of accuracy. *INDEX TERMS:* 0644 Electromagnetics: Numerical methods; 0669 Electromagnetics: Scattering and diffraction; 0684 Electromagnetics: Transient and time domain; *KEYWORDS:* two-dimensional finite difference time domain, global transparent boundary conditions, plane-wave-time-domain algorithm

Citation: Lu, M., M. Lv, A. A. Ergin, B. Shanker, and E. Michielssen (2004), Multilevel plane wave time domain–based global boundary kernels for two-dimensional finite difference time domain simulations, *Radio Sci.*, *39*, RS4007, doi:10.1029/2003RS002928.

1. Introduction

[2] Finite difference time domain (FDTD) schemes are widely used to analyze electromagnetic transients in penetrable, inhomogeneous, and nonlinear media [*Taflove*, 1995]. FDTD methods discretize Maxwell's differential equations by approximating all spatial and temporal derivatives by finite differences. The popular Yee FDTD scheme uses spatially staggered grids to discretize electric and magnetic fields and a leapfrog scheme to advance the fields in time [*Yee*, 1966]. When applied to the analysis of open region, free-space, scattering and radiation transients, these spatial grids somehow must be truncated. The boundary condition imposed on the truncation interface must accurately account for the presence of an unbounded free-space exterior medium.

[3] In the past, both local absorbing and global transparent boundary conditions (ABCs and TBCs) have been used to truncate FDTD meshes. ABCs enforce so-called one-way wave equations or numerically dissipate impinging waves. Early ABCs include those formulated by *Engquist and Majda* [1977], *Higdon* [1987], *Mur* [1981], and *Liao et al.* [1984]; recent developments are the complementary operators by *Wu and Ramahi* [2002] and the perfectly matched layer (PML) originally devised by Berenger and subsequently refined by others [*Berenger*, 1994; *Chew and Weedon*, 1994; *Chew et al.*, 1997]. These local ABCs apply only to convex outer boundaries and should be deployed several FDTD cells away from the scatterer (Figure 1a). In contrast, global TBCs rely on Huygens' principle to facilitate the transition from the FDTD grid to its free-space surroundings

0048-6604/04/2003RS002928

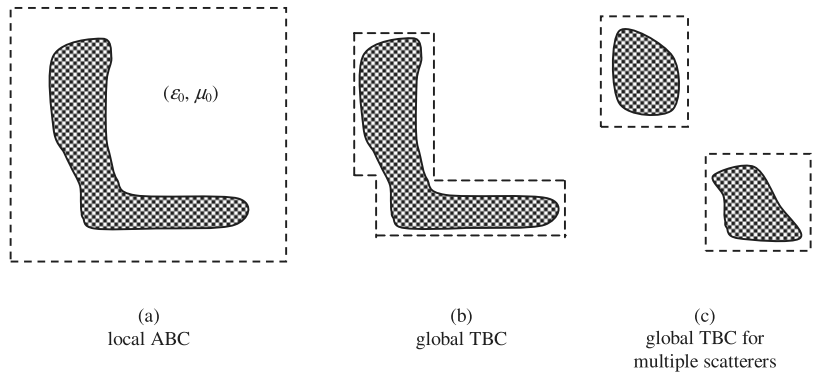

Figure 1. Comparison between local ABC and global TBC.

(for a representative, though nonexhaustive collection of papers on this topic, see *Ziolkowski et al.* [1983], *Ting and Miksis* [1986], *Keller and Givoli* [1989], *Oliver* [1992], *De Moerloose and De Zutter* [1993], *Johnson and Rahmat-Samii* [1997], *Djordjevic et al.* [1995], *Givoli and Cohen* [1995], *Grote and Keller* [1998], *Alpert et al.* [2000], *Grote and Keller* [2000], *Holtzman and Kastner* [2001], and *Lubich and Schadle* [2002]). Unlike local ABCs, the application of global TBCs is not restricted by the shape of the FDTD boundary. Global TBCs can be shrink-wrapped around the scatterer, minimizing the volume of the FDTD domain (Figure 1b). This advantage is especially significant when analyzing scattering from disjoint inhomogeneities. Indeed, global TBCs permit each inhomogeneity to be discretized using separate FDTD grids that communicate with each other through their surfaces [*Johnson and Rahmat-Samii*, 1997; *Bernardi et al.*, 2002] (Figure 1c). Unfortunately, global TBCs are not the end-all method as they suffer from a high computational complexity. This is the primary reason why they have not been widely adopted by the computational electromagnetics community.

[4] This paper outlines a new scheme to reduce the computational cost associated with the use of global TBC kernels in two-dimensional (2-D) FDTD simulations. The proposed scheme relies on the 2-D plane wave time domain (PWTD) algorithm to compute scattered fields generated by equivalent sources residing on the FDTD grid boundary. Consider a 2-D FDTD mesh on the surface of which equivalent sources are represented by their samples at $\tilde{N}^s$ spatial boundary nodes for a total of $\tilde{N}^t$ time steps. The computational cost associated with the evaluation of global TBC kernel scales as $O(\tilde{N}^{s^2}\tilde{N}^{t^2})$. This cost is reduced to $O(\tilde{N}^s\tilde{N}^t \log \tilde{N}^s \log \tilde{N}^t)$ by using the proposed 2-D multilevel PWTD scheme. Moreover, the PWTD accelerator does so without foregoing the previously mentioned advantages of the TBC or compromising the accuracy of the underlying TBC kernel. It is to be noted that this is not the first attempt at constructing a fast TBC kernel. Recently, *Grote and Keller* [1998], *Alpert et al.* [2000], and *Lubich and Schadle* [2002] developed fast TBC kernels for planar/cylindrical/spherical truncation boundaries that are highly competitive with PML schemes. Our fast scheme differs from theirs in that it applies to arbitrarily shaped outer boundaries, including concave ones. While the presentation focuses on TBCs for Yee FDTD schemes, the same methodology applies, with only minor modifications, to the construction of fast global TBCs for higher-order FDTD and finite element time domain solvers.

[5] This paper is organized as follows. Section 2 outlines the construction of a PWTD-accelerated global TBC kernel for a 2-D FDTD solver. Section 3 describes several numerical examples that validate the proposed technique and demonstrate its accuracy and efficiency. Finally, section 4 contains conclusions to this study.

2. PWTD-Enhanced Global TBC for 2-D FDTD

[6] This section outlines the construction of a PWTD-accelerated global TBC kernel for the 2-D FDTD simulation of transverse magnetic to z (TM_z) electromagnetic field phenomena. By duality the proposed TBC kernel also applies to the study of transverse electric to z field transients. The construction of a global, combined field TBC kernel for a 2-D Yee FDTD solver is outlined in section 2.1. The PWTD-based acceleration of this kernel is described in section 2.2.

2.1. Global TBC for 2-D FDTD

[7] Consider a penetrable and z (axially)-invariant scatterer of permittivity $\varepsilon(\boldsymbol{\rho})$ and permeability $\mu(\boldsymbol{\rho})$, with $\boldsymbol{\rho} = \hat{\mathbf{x}}x + \hat{\mathbf{y}}y$, residing in a domain Ω^s (Figure 2). Outside Ω^s there is only free-space, i.e., $\varepsilon(\boldsymbol{\rho}) = \varepsilon_0$ and $\mu(\boldsymbol{\rho}) = \mu_0$ for $\boldsymbol{\rho} \notin \Omega^s$. In what follows, it is assumed that Ω^s is hierarchically embedded within two other domains: Ω^h and Ω^e. The boundary of Ω^r, $r \in \{s, h, e\}$, is denoted

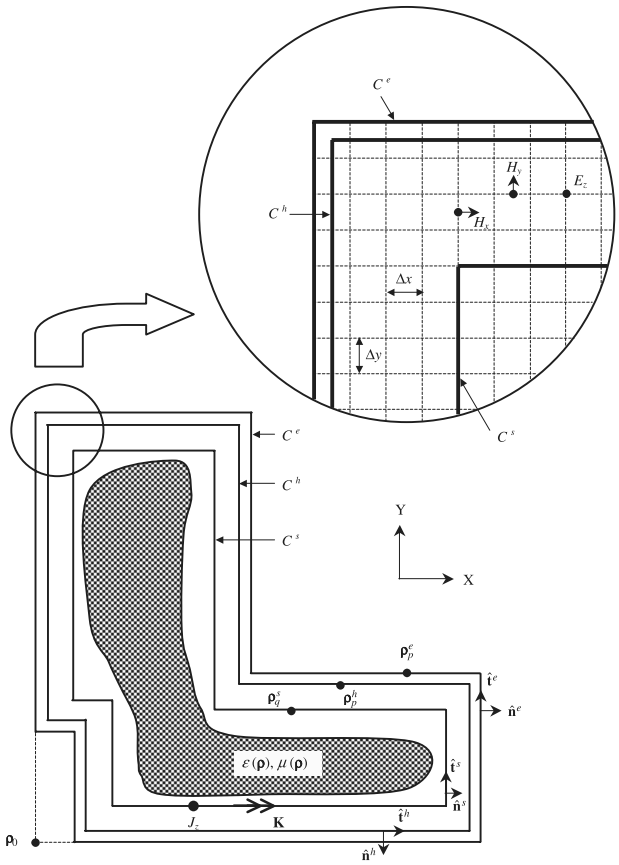

Figure 2. Illustration of the global boundaries.

by C^r and its length by $|C^r|$. Additionally, transverse outward pointing and tangential unit vectors to C^r are denoted $\hat{\mathbf{n}}^r(\boldsymbol{\rho})$ and $\hat{\mathbf{t}}^r(\boldsymbol{\rho}) = \hat{\mathbf{z}} \times \hat{\mathbf{n}}^r(\boldsymbol{\rho})$, respectively.

[8] The electromagnetic field in Ω^s is excited by a z-invariant impressed current $\hat{\mathbf{z}}J_z^e(\boldsymbol{\rho}, t)$. This excitation is (approximately) temporally bandlimited to $\omega_{\max} = 2\pi c/\lambda_{\min}$, where $c = 1/\sqrt{\mu_0\varepsilon_0}$ is the free-space speed of light, and $\lambda_{\min}$ is the free-space wavelength at $\omega = \omega_{\max}$. The electromagnetic field ($\mathbf{E}(\boldsymbol{\rho}, t) = \hat{\mathbf{z}}E_z(\boldsymbol{\rho}, t)$, $\mathbf{H}(\boldsymbol{\rho}, t) = \hat{\mathbf{x}}H_x(\boldsymbol{\rho}, t) + \hat{\mathbf{y}}H_y(\boldsymbol{\rho}, t)$) due to $\hat{\mathbf{z}}J_z^e(\boldsymbol{\rho}, t)$ satisfies

$$\begin{aligned}
\varepsilon(\boldsymbol{\rho})\frac{\partial E_z(\boldsymbol{\rho},t)}{\partial t} &= \frac{\partial H_y(\boldsymbol{\rho},t)}{\partial x} - \frac{\partial H_x(\boldsymbol{\rho},t)}{\partial y} - J_z^e(\boldsymbol{\rho},t)\\
\mu(\boldsymbol{\rho})\frac{\partial H_x(\boldsymbol{\rho},t)}{\partial t} &= -\frac{\partial E_z(\boldsymbol{\rho},t)}{\partial y}\\
\mu(\boldsymbol{\rho})\frac{\partial H_y(\boldsymbol{\rho},t)}{\partial t} &= \frac{\partial E_z(\boldsymbol{\rho},t)}{\partial x},
\end{aligned} \tag{1}$$

and is assumed to (essentially) vanish throughout Ω^e for $t < 0$.

[9] Equation (1) is solved for $E_z(\boldsymbol{\rho}, t)$, $H_x(\boldsymbol{\rho}, t)$, and $H_y(\boldsymbol{\rho}, t)$ using the standard Yee-scheme. This necessitates that the aforementioned domains, boundaries, and equations are discretized. From here on, all symbols refer to discretized quantities unless specifically stated otherwise. Staggered primary and secondary grids are superimposed on Ω^e, as shown in Figure 2. The primary grid is anchored to $\boldsymbol{\rho}_0 = \hat{\mathbf{x}}x_0 + \hat{\mathbf{y}}y_0$ and has cell sizes Δx and Δy along x and y, respectively; typically, $\Delta x = \Delta y$. The secondary grid is anchored to $\boldsymbol{\rho}_0' = \hat{\mathbf{x}}x_0' + \hat{\mathbf{y}}y_0'$, where $x_0' = x_0 + 0.5\Delta x$ and $y_0' = y_0 + 0.5\Delta y$, and has identical cell sizes. Next, electric fields $E_z(\boldsymbol{\rho}, t)$ are sampled on the nodes of the primary grid at times $t = t_l = l\Delta t$, $l = 1,\ldots,N^t$, where Δt is the time step size and N^t is the number of time steps. The analysis spans $T = N^t\,\Delta t$ seconds. Similarly, magnetic fields $H_x(\boldsymbol{\rho}, t)$ and $H_y(\boldsymbol{\rho}, t)$ are sampled at the centers of, and along, the x- and y- directed edges of the secondary grid at times $t = \tilde{t}_l = (l + 1/2)\,\Delta t$:

$$\begin{aligned}
E^l_{z,(i,j)} &= E_z(\hat{\mathbf{x}}(i\Delta x + x_0) + \hat{\mathbf{y}}(j\Delta y + y_0), t_l),\\
&\quad 0 \le i \le N_x, 0 \le j \le N_y,
\end{aligned} \tag{2}$$

$$\begin{aligned}
H^l_{x,(i,j)} &= H_x(\hat{\mathbf{x}}(i\Delta x + x_0) + \hat{\mathbf{y}}((j + 0.5)\Delta y + y_0), \tilde{t}_l),\\
&\quad 0 \le i \le N_x, 0 \le j \le N_y - 1,
\end{aligned} \tag{3}$$

$$\begin{aligned}
H^l_{y,(i,j)} &= H_y(\hat{\mathbf{x}}((i + 0.5)\Delta x + x_0) + \hat{\mathbf{y}}(j\Delta y + y_0), \tilde{t}_l),\\
&\quad 0 \le i \le N_x - 1, 0 \le j \le N_y,
\end{aligned} \tag{4}$$

and $\boldsymbol{\rho} \in \Omega^e$. Using the above definitions, the FDTD update equations read:

$$\begin{aligned}
E^l_{z,(i,j)} &= E^{l-1}_{z,(i,j)} + \frac{\Delta t}{\varepsilon(\hat{\mathbf{x}}(i\Delta x + x_0) + \hat{\mathbf{y}}(j\Delta y + y_0))}\\
&\quad \cdot \left(\frac{1}{\Delta x}\left(H^{l-1}_{y,(i,j)} - H^{l-1}_{y,(i-1,j)}\right)\right.\\
&\quad \left. - \frac{1}{\Delta y}\left(H^{l-1}_{x,(i,j)} - H^{l-1}_{x,(i,j-1)}\right) - J_z^e(\hat{\mathbf{x}}(i\Delta x + x_0)\right.\\
&\quad \left. + \hat{\mathbf{y}}(j\Delta y + y_0), \tilde{t}_{l-1})\right)\\
H^l_{x,(i,j)} &= H^{l-1}_{x,(i,j)} - \frac{\Delta t}{\Delta y}\\
&\quad \cdot \frac{1}{\mu(\hat{\mathbf{x}}(i\Delta x + x_0) + \hat{\mathbf{y}}((j + 0.5)\Delta y + y_0))}\\
&\quad \cdot \left(E^l_{z,(i,j+1)} - E^l_{z,(i,j)}\right)\\
H^l_{y,(i,j)} &= H^{l-1}_{y,(i,j)} + \frac{\Delta t}{\Delta x}\\
&\quad \cdot \frac{1}{\mu(\hat{\mathbf{x}}((i + 0.5)\Delta x + x_0) + \hat{\mathbf{y}}(j\Delta y + y_0))}\\
&\quad \cdot \left(E^l_{z,(i+1,j)} - E^l_{z,(i,j)}\right).
\end{aligned} \tag{5}$$

In what follows, it is assumed that (the discretized) C^s and C^e reside on the primary grid, while the discretized C^h tracks the secondary grid. Typically, C^h resides half a cell within C^e, and C^s is separated from C^h by just a few cells. Field sampling points on C^r, $r \in \{s, h, e\}$, are numbered sequentially by traversing C^r in a counterclockwise direction; they number N^r and are located at $\boldsymbol{\rho}_q^r$, $q = 1,\ldots, N^r$. As all three boundaries reside close to one another, $N^s \simeq N^h \simeq N^e$; this condition is assumed to hold true from here on. Mappings from the q to FDTD field point (i, j) indices are denoted $(i^r(q), j^r(q))$. Finally, it is also assumed that the scatterer has no fine geometric features that control the spatial discretization. This assumption ensures (1) that the boundaries C^r are relatively smooth (which is important in the discretization of the boundary integrals to be introduced shortly) and (2) that Δx and Δy are typically around $\lambda_{\min}/20$ when the scatterer is electrically large (which is sufficient for most engineering applications) and become smaller only when required to control grid dispersion. Given the grid dispersion characteristics of the Yee scheme, this implies that N^r is of $O((|C^r|/\lambda_{\min})^{\alpha})$ with $\alpha = 3/2$ [*Chew*, 1995]. (This guarantees that the phase dispersion error incurred for a fixed number of trips of the field across the scatterer region is controlled and therefore does not guarantee accuracy in resonant scenarios; also, if a higher-order finite difference scheme were used, the exponent α would be smaller.)

[10] Electric fields at points on boundary C^e, $E^l_{z,[i^e(q),j^e(q)]} = E_z(\boldsymbol{\rho}_q^e, l\Delta t)$, $q = 1, 2,\ldots, N^e$, cannot be updated using the Yee equations (5) as these require knowledge of magnetic fields outside C^e. The scattered electric and magnetic fields however do satisfy the Sommerfeld radiation condition for $|\boldsymbol{\rho}| \to \infty$; that is, if C^s is convex, then the scattered fields outside C^s can be described as "outward going". This condition often is exploited to permit computation of the boundary fields by wrapping Ω^s within a so-called PML, viz. a layer that absorbs all energy incident upon it, and within which fields rapidly decay, thereby providing a natural termination to the computational domain [*Berenger*, 1994; *Chew and Weedon*, 1994; *Chew et al.*, 1997]. Alternatively, however, it is possible to exploit surface equivalence principles (EPs) to truncate the computational domain. Indeed, knowledge of electric and magnetic fields tangential to C^s permits the computation of scattered fields everywhere outside C^s, including for $\boldsymbol{\rho} \in C^e$. Use of surface EPs to truncate the computational domain removes the requirement that the boundary be convex. The implementation of EP-based boundary kernels is detailed next.

[11] The EPs state that fields at points on the boundary, $E^l_{z,[i^e(q),j^e(q)]} = E_z(\boldsymbol{\rho}_q^e, l\Delta t)$, $q = 1,\ldots, N^e$, can be represented as those radiated by sources residing in free space. The sources include impressed currents that reside ouside C^s, and equivalent electric and magnetic surface currents $J_z(\boldsymbol{\rho}, t)$ and $\mathbf{K}(\boldsymbol{\rho}, t)$ on C^s defined by

$$J_z(\boldsymbol{\rho}, t) = \hat{\mathbf{z}} \cdot [\hat{\mathbf{n}}^s(\boldsymbol{\rho}) \times \mathbf{H}(\boldsymbol{\rho}, t)] \quad \boldsymbol{\rho} \in C^s, \tag{6}$$

$$\mathbf{K}(\boldsymbol{\rho}, t) = \hat{\mathbf{t}}^s(\boldsymbol{\rho}) E_z(\boldsymbol{\rho}, t) \qquad \boldsymbol{\rho} \in C^s. \tag{7}$$

In our TBC scheme, the EPs are used not only to express electric fields on C^e but also to partially compute magnetic fields on C^h. This is necessary to prevent the excitation of non-unique solutions associated with the imposition of so-called pure electric- or magnetic field boundary conditions. As was shown in the work of *Lu et al.* [2004a], imposing a combination of electric and magnetic field boundary conditions eliminates the buildup of all spurious modes. It follows from the EPs that total axial electric fields on C^e and transverse magnetic fields tangential to C^h can be represented as

$$\begin{aligned} E_z[\mathrm{EP}](\boldsymbol{\rho}, t) = & -\mu_0 \int_{C^s} (\partial_t J_z(\boldsymbol{\rho}', t)) * g(|\boldsymbol{\rho} - \boldsymbol{\rho}'|, t) d\boldsymbol{\rho}' \\ & - \hat{\mathbf{z}} \cdot \nabla \times \int_{C^s} \mathbf{K}(\boldsymbol{\rho}', t) * g(|\boldsymbol{\rho} - \boldsymbol{\rho}'|, t) d\boldsymbol{\rho}' \\ & + E_z^i(\boldsymbol{\rho}, t) \qquad \boldsymbol{\rho} \in C^e, \end{aligned} \tag{8}$$

$$\begin{aligned} \hat{\mathbf{t}}^h(\boldsymbol{\rho}) \cdot \mathbf{H}[\mathrm{EP}](\boldsymbol{\rho}, t) = & \hat{\mathbf{t}}^h(\boldsymbol{\rho}) \cdot \nabla \times \hat{\mathbf{z}} \int_{C^s} d\boldsymbol{\rho}' J_z(\boldsymbol{\rho}', t) \\ & * g(|\boldsymbol{\rho} - \boldsymbol{\rho}'|, t) - \hat{\mathbf{t}}^h(\boldsymbol{\rho}) \cdot \varepsilon_0 \int_{-\infty}^{t} dt' \\ & \cdot \left(\partial_{t'}^2 \bar{\mathbf{I}} - c^2 \nabla\nabla\right) \cdot \int_{C^s} d\boldsymbol{\rho}' \mathbf{K}(\boldsymbol{\rho}', t') \\ & * g(|\boldsymbol{\rho} - \boldsymbol{\rho}'|, t') + \hat{\mathbf{t}}^h(\boldsymbol{\rho}) \cdot \mathbf{H}^i(\boldsymbol{\rho}, t) \\ & \boldsymbol{\rho} \in C^h, \end{aligned} \tag{9}$$

where a reference to "[EP]" behind a field quantity implies it has been "obtained from the equivalence principle", and $(\mathbf{E}^i(\boldsymbol{\rho}, t) = \hat{\mathbf{z}} E_z^i(\boldsymbol{\rho}, t), \mathbf{H}^i(\boldsymbol{\rho}, t))$ are impressed electric and magnetic fields (i.e., the fields produced by all impressed sources residing external to C^s when radiating in free space), the star denotes a temporal convolution, $g(\cdot, \cdot)$ is the 2-D free-space time domain Green function

$$g(\rho, t) = \frac{1}{2\pi} \frac{u(t - \rho/c)}{\sqrt{t^2 - (\rho/c)^2}}, \tag{10}$$

and $u(\cdot)$ denotes the Heaviside step function

$$u(x) = \begin{cases} 0 & x < 0 \\ 1 & x \geq 0 \end{cases}. \tag{11}$$

In our global TBC scheme, electric and magnetic fields on C^e and C^h are updated using

$$E^l_{z,[i^e(p),j^e(p)]} = E_z[\mathrm{EP}]\left(\boldsymbol{\rho}^e_p, t_l\right) \quad p = 1, \ldots, N^e, \tag{12}$$

$$\begin{aligned} H^l_{x,[i^h(p),j^h(p)]} = {} & \alpha H^l_{x,[i^h(p),j^h(p)]}[\mathrm{FDTD}] + (1-\alpha)\hat{\mathbf{t}}^h\left(\boldsymbol{\rho}^h_p\right) \\ & \cdot \mathbf{H}[\mathrm{EP}]\left(\boldsymbol{\rho}^h_p, \tilde{t}_l\right) \quad p = 1, \ldots, N^h, \\ & \text{provided that } \hat{\mathbf{t}}^h\left(\boldsymbol{\rho}^h_p\right) = \hat{\mathbf{x}}, \end{aligned} \tag{13}$$

$$\begin{aligned} H^l_{y,[i^h(p),j^h(p)]} = {} & \alpha H^l_{y,[i^h(p),j^h(p)]}[\mathrm{FDTD}] + (1-\alpha)\hat{\mathbf{t}}^h\left(\boldsymbol{\rho}^h_p\right) \\ & \cdot \mathbf{H}[\mathrm{EP}]\left(\boldsymbol{\rho}^h_p, \tilde{t}_l\right) \quad p = 1, \ldots, N^h, \\ & \text{provided that } \hat{\mathbf{t}}^h\left(\boldsymbol{\rho}^h_p\right) = \hat{\mathbf{y}}. \end{aligned} \tag{14}$$

Here, $H^l_{x,(i,j)}$ [FDTD] and $H^l_{y,(i,j)}$ [FDTD] denote magnetic field components computed using equation (5), i.e., using the FDTD update equations, and $0 < \alpha < 1$. If $\alpha = 1$, the scheme would update magnetic field on C^h entirely using FDTD rules. In contrast, if $\alpha = 0$, the scheme would express magnetic field values on C^h exclusively as those produced by J_z ($\boldsymbol{\rho}$, t) and $\mathbf{K}$($\boldsymbol{\rho}$, t); in this case equation (12) becomes superfluous. Neither $\alpha = 1$ nor $\alpha = 0$ are good choices, because the resulting solvers are prone to buildup of resonant modes in cavities with perfect electrically or magnetically conducting walls coinciding with C^e or C^h, respectively. In practice, therefore, we chose $0 < \alpha < 1$ (and typically $\alpha \approx 1/2$) because doing so eliminates the buildup of resonant modes inside the computational domain; the resulting boundary condition will henceforth be referred to as the combined field TBC. The resonant modes problem associated with the global TBC is discussed in detail in another paper [*Lu et al.*, 2004a].

[12] Care should be taken in the manner in which J_z ($\boldsymbol{\rho}$, t) and $\mathbf{K}$($\boldsymbol{\rho}$, t) on C^s is computed, and how the boundary integrals in equations (8) and (9) are discretized. Accurate and efficient evaluation of equations (8) and (9) requires the integrals to be discretized in terms of $\tilde{N}^s$ quadrature points with $\tilde{N}^s$ of $O(|C^s|/\lambda_{\min})$. Because N^s scales as $O(|C^s/\lambda_{\min}|^{1.5})$ [*Chew*, 1995], efficient evaluation of the boundary integrals cannot be achieved by letting the quadrature points coincide with the equispaced FDTD nodes on C^s. In practice, to define J_z ($\boldsymbol{\rho}$, t) and $\mathbf{K}$($\boldsymbol{\rho}$, t) on C^s, field data from $O(N^s)$ FDTD grid points are locally interpolated to $\tilde{N}^s$ quadrature points $\tilde{\boldsymbol{\rho}}^s_p$, $p = 1, \ldots, \tilde{N}^s$ on C^s at a cost that scales as $O(\tilde{N}^s)$. The process is repeated, in reverse, for the observers. That is, instead of directly computing the electric and magnetic fields due to the sources J_z ($\boldsymbol{\rho}$, t) and $\mathbf{K}$($\boldsymbol{\rho}$, t) for all $\boldsymbol{\rho}^h_p$, $p = 1, \ldots, N^h$ and $\boldsymbol{\rho}^e_p$, $p = 1, \ldots, N^e$, these fields are computed on sparser grids defined by points $\tilde{\mathbf{r}}^h_p$, $p = 1, \ldots, \tilde{N}^h$ and $\tilde{\mathbf{r}}^e_p$, $p = 1, \ldots, \tilde{N}^e$ with $\tilde{N}^s \approx \tilde{N}^h \approx \tilde{N}^e$ and then interpolated to all FDTD grid points at a cost of $O(N^h) = O(N^e)$. It should be noted that, in the above procedure, FDTD updates and boundary field evaluation proceed virtually independent of one another; hence the Yee scheme can be replaced by other FDTD or finite element time domain algorithms without affecting the operation of the boundary kernel. In summary, interpolation aside, the task of updating the boundary FDTD fields reduces to computing

$$\begin{aligned} & \left[-\mu_0 \int_{C^s} (\partial_t J_z(\boldsymbol{\rho}', t)) * g(|\boldsymbol{\rho} - \boldsymbol{\rho}'|, t) d\boldsymbol{\rho}' \right. \\ & \left. -\hat{\mathbf{z}} \cdot \nabla \times \int_{C^s} \mathbf{K}(\boldsymbol{\rho}', t) * g(|\boldsymbol{\rho} - \boldsymbol{\rho}'|, t) d\boldsymbol{\rho}' \right]_{\boldsymbol{\rho} = \tilde{\boldsymbol{\rho}}^e_p} \\ & \cong \left[-\mu_0 \sum_{q=1}^{\tilde{N}^s} w_q \left(\partial_t J_z\left(\tilde{\boldsymbol{\rho}}^s_q, t\right)\right) * g\left(|\boldsymbol{\rho} - \tilde{\boldsymbol{\rho}}^s_q|, t\right) \right. \\ & \left. -\hat{\mathbf{z}} \cdot \nabla \times \sum_{q=1}^{\tilde{N}^s} w_q \mathbf{K}\left(\tilde{\boldsymbol{\rho}}^s_q, t\right) * g\left(|\boldsymbol{\rho} - \tilde{\boldsymbol{\rho}}^s_q|, t\right) \right]_{\boldsymbol{\rho} = \tilde{\boldsymbol{\rho}}^e_p} \\ & = \sum_{q=1}^{\tilde{N}^s} E_{pq}(t) \qquad p = 1, \ldots, \tilde{N}^e, \end{aligned} \tag{15}$$

$$\begin{aligned} & \left[\hat{\mathbf{t}}^h(\boldsymbol{\rho}) \cdot \nabla \times \hat{\mathbf{z}} \int_{C^s} d\boldsymbol{\rho}' J_z(\boldsymbol{\rho}', t) * g(|\boldsymbol{\rho} - \boldsymbol{\rho}'|, t) - \hat{\mathbf{t}}^h(\boldsymbol{\rho}) \right. \\ & \cdot \varepsilon_0 \int_{-\infty}^{t} dt' \left(\partial_{t'}^2 \bar{\mathbf{I}} - c^2 \nabla\nabla\right) \cdot \int_{C^s} d\boldsymbol{\rho}' \mathbf{K}(\boldsymbol{\rho}', t') \\ & \left. * g(|\boldsymbol{\rho} - \boldsymbol{\rho}'|, t') \right]_{\boldsymbol{\rho} = \tilde{\boldsymbol{\rho}}^h_p} \\ & \cong \left[\hat{\mathbf{t}}^h(\boldsymbol{\rho}) \cdot \nabla \times \hat{\mathbf{z}} \sum_{q=1}^{\tilde{N}^s} w_q J_z\left(\tilde{\boldsymbol{\rho}}^s_q, t\right) * g\left(|\boldsymbol{\rho} - \tilde{\boldsymbol{\rho}}^s_q|, t\right) \right. \\ & -\mathbf{t}^h(\boldsymbol{\rho}) \cdot \varepsilon_0 \int_{-\infty}^{t} dt' \left(\partial_{t'}^2 \bar{\mathbf{I}} - c^2 \nabla\nabla\right) \cdot \sum_{q=1}^{\tilde{N}^s} w_q \mathbf{K}\left(\tilde{\boldsymbol{\rho}}^s_q, t'\right) \\ & \left. * g\left(|\boldsymbol{\rho} - \tilde{\boldsymbol{\rho}}^s_q|, t'\right) \right]_{\boldsymbol{\rho} = \tilde{\boldsymbol{\rho}}^h_p} \\ & = \sum_{q=1}^{\tilde{N}^s} H_{pq}(t) \qquad p = 1, \ldots, \tilde{N}^h, \end{aligned} \tag{16}$$

where w_q, $q = 1,\ldots, \tilde{N}^s$ are quadrature weights, and all $\tilde{N}^r$ are of order $O(|C^s|/\lambda_{\min})$. The above equations also implicitly define $E_{pq}(t)$ and $H_{pq}(t)$ for future use.

[13] Each temporal convolution in equations (15) and (16) requires, on average, $O(\tilde{N}^t = \chi_t T \omega_{\max})$ temporal samples (spaced $\Delta\tilde{t}$ apart) of the currents and floating point operations. Here, χ_t is an oversampling factor that typically ranges between 2 and 4 and that equals 1 when signals are sampled at the Nyquist rate. It is assumed here that the minimal distance between C^s and C^e is at least $\Delta\tilde{t}$ as this implies that the boundary updates can be affected using historical values of the current; hence, the FDTD update remains explicit. Note that, contrary to Δt, $\Delta\tilde{t}$ does not scale with the size of the scatterer. Indeed, when the scatterer dimensions grow and grid dispersion calls for spatial grid refinement, the FDTD time step has to shrink in accordance with the CFL condition [*Taflove*, 1995], and hence $N^t = O(\tilde{N}^{t^{(3/2)}})$. Again, the exponent would be smaller if higher-order FDTD schemes were used. This implies that, in addition to the above discussed spatial interpolation, temporal interpolation is called for, again on both the source and observer surfaces. In practice, both spatial and temporal sub-sampling is often achieved by dropping FDTD samples. It is then easily verified that the evaluation of equations (15) and (16) for all $\tilde{N}^t$ time points requires $O(\tilde{N}^{s^2}\tilde{N}^{t^2})$ operations. This high computational cost prevents the global TBCs from being widely used. However, this cost can be reduced to $O(\tilde{N}^s\tilde{N}^t \log \tilde{N}^s \log \tilde{N}^t)$ by using the multilevel 2-D PWTD scheme described next.

2.2. PWTD Acceleration for the Evaluation of the Global TBC

[14] This section outlines the application of the 2-D PWTD scheme to the evaluation of the fields E_z [EP]$(\tilde{\boldsymbol{\rho}}_p^e, t)$ and $\mathbf{H}$[EP]$(\tilde{\boldsymbol{\rho}}_p^h, t)$. The PWTD algorithm constitutes a three-stage algorithm for evaluating transient fields generated by bandlimited sources and can be considered the extension to the time domain of the frequency domain (Helmholtz equation) fast multipole algorithm [*Coifman et al.*, 1993; *Song et al.*, 1997]. The procedure derives its computational efficiency from a plane wave representation of the scalar Green function $g(\rho, t)$ in equation (10). The reader is encouraged to consult reference [*Lu et al.*, 2000], as it provides a complete description of the 2-D PWTD scheme, including details pertaining to its implementation and convergence. In what follows, the scheme's modus operandi is summarized and special attention is paid to the extensions required for it to become applicable to the problem at hand.

[15] To apply the multilevel 2-D PWTD algorithm to compute E_z [EP]$(\tilde{\boldsymbol{\rho}}_p^e, t)$ and $\mathbf{H}$[EP]$(\tilde{\boldsymbol{\rho}}_p^h, t)$, all the three boundaries C^s, C^h, and C^e are enclosed within a fictitious square box, as shown in Figure 3 (in Figure 3, C^s, C^h, and C^e are represented by one line). The fictitious square box is then hierarchically subdivided into smaller boxes until the smallest boxes thus obtained measure approximately $\lambda_{\min}$ on the side; i.e., the smallest boxes contain $O(1)$ discrete source and integration points. Boxes containing no points $\tilde{\boldsymbol{\rho}}_p^r$ are discarded in the process. The smallest boxes are said to reside on level 1; the large box containing all C^r is said to reside on level N_l, which is of $O(\log \tilde{N}^s)$. Next, all "interactions" between sources at points $\tilde{\boldsymbol{\rho}}_q^s$, $q = 1,\ldots, \tilde{N}^s$ and observers at points $\tilde{\boldsymbol{\rho}}_p^h$, $p = 1,\ldots, \tilde{N}^h$ and $\tilde{\boldsymbol{\rho}}_p^e$, $p = 1,\ldots, \tilde{N}^e$ are uniquely attributed to a pair of boxes, as follows. Starting at level $N_l - 2$ and descending to level 1, all level i far-field box pairs of nonempty boxes are identified. A level i far-field box pair comprises two boxes (1) that do not touch and (2) whose interactions are not accounted for at a higher level. It follows that interactions not accounted for by far-field box pairs are between level 1 boxes that touch one another; they are termed near-field interactions (Figure 3).

[16] It can be shown that the Hilbert transform of the propagating plane wave spectrum of the Green function $g(\boldsymbol{\rho}, t)$, when convolved with a source temporal signature, yields the source's fields outside the source domain after the source has stopped radiating. The 2-D PWTD scheme exploits this fact to compute interaction between far field box pairs at all levels. To this end, the source signatures are subdivided into N_v temporally consecutive subsignals, each of which is bandlimited and approximately time-limited. Consequently, the field due to the unsplit sources is a linear superposition of fields due to N_v subsignals. Note, a linear superposition of plane waves results in causal and anti-causal terms (henceforth referred to as the ghost signals). Conditions that permit time gating of the ghost signal are described below. The artificial split of the source function is illustrated in Figure 4, and is described in detail in the work of *Lu et al.* [2000]. The field signatures due to these subsignals are split accordingly; i.e., upon defining $J_q(t) = J_z(\tilde{\boldsymbol{\rho}}_q^s, t)$ and $K_q(t) = \mathbf{K}(\tilde{\boldsymbol{\rho}}_q^s, t) \cdot \hat{\mathbf{t}}^s(\tilde{\mathbf{r}}_q^s)$, we have

$$J_q(t) = \sum_{v=1}^{N_v} J_{q,v}(t) \qquad K_q(t) = \sum_{v=1}^{N_v} K_{q,v}(t) \tag{17}$$

$$E_{pq}(t) = \sum_{v=1}^{N_v} E_{pq,v}(t) \qquad H_{pq}(t) = \sum_{v=1}^{N_v} H_{pq,v}(t), \tag{18}$$

where

$$\begin{aligned} E_{pq,v}(t) = {} & -w_q \mu_0 \partial_t \left[J_{q,v}(t) * g\left(|\boldsymbol{\rho} - \tilde{\boldsymbol{\rho}}_q^s|, t\right)\right]_{\boldsymbol{\rho}=\tilde{\boldsymbol{\rho}}_p^e} \\ & -w_q \hat{\mathbf{z}} \cdot \left[\nabla \times \hat{\mathbf{t}}^s\left(\tilde{\boldsymbol{\rho}}_q^s\right) K_{q,v}(t) * g\left(|\boldsymbol{\rho} - \tilde{\boldsymbol{\rho}}_q^s|, t\right)\right]_{\boldsymbol{\rho}=\boldsymbol{\rho}_p^e}, \end{aligned} \tag{19}$$

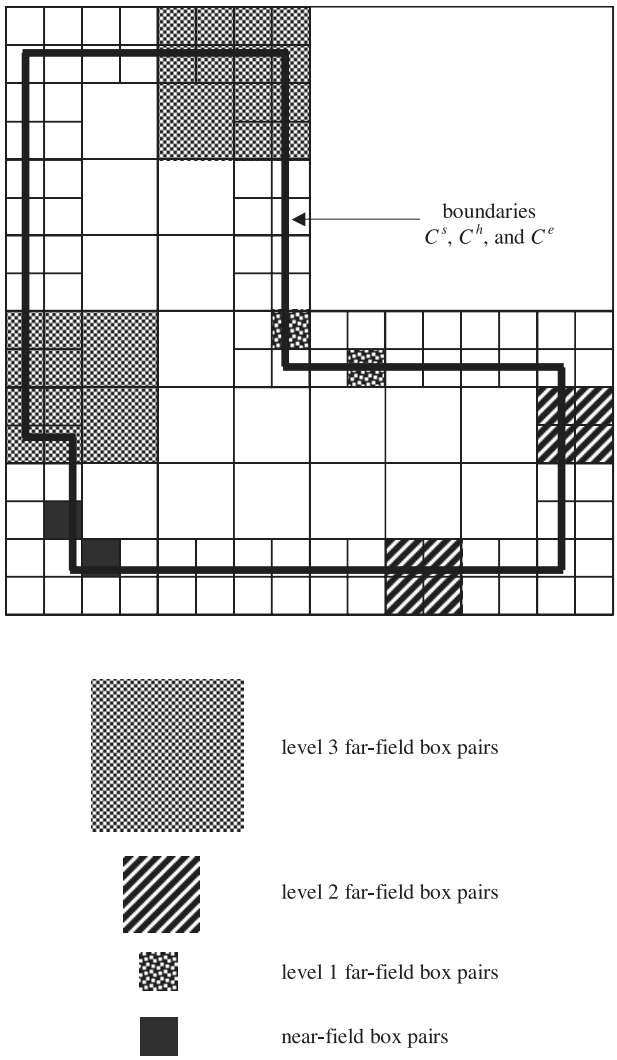

Figure 3. Illustration of the multilevel subdivision of the geometry.

$$H_{pq,v}(t) = \left[w_q \hat{\mathbf{t}}^h(\boldsymbol{\rho}) \cdot \nabla \times \hat{\mathbf{z}} J_{q,v}(t) * g\left(|\boldsymbol{\rho} - \tilde{\boldsymbol{\rho}}_q^s|, t \right) \right]_{\boldsymbol{\rho}=\tilde{\boldsymbol{\rho}}_p^h} - \left[w_q \hat{\mathbf{t}}^h(\boldsymbol{\rho}) \cdot \varepsilon_0 \int_{-\infty}^{t} dt' \left(\partial_{t'}^2 \bar{\mathbf{I}} - c^2 \nabla\nabla \right) \cdot \hat{\mathbf{t}}\left(\tilde{\boldsymbol{\rho}}_q^s \right) K_{q,v}(t') * g\left(|\boldsymbol{\rho} - \tilde{\boldsymbol{\rho}}_q^s|, t' \right) \right]_{\boldsymbol{\rho}=\tilde{\boldsymbol{\rho}}_p^h}. \quad (20)$$

To use the PWTD scheme to compute $E_{pq,v}(t)$ and $H_{pq,v}(t)$, assume that points $\tilde{\boldsymbol{\rho}}_q^s$ and $\tilde{\boldsymbol{\rho}}_q^e$ belong to a far-field pair of boxes with circumscribing radius R_s. Let $\tilde{\boldsymbol{\rho}}_{q,c}^s$ and $\tilde{\boldsymbol{\rho}}_{p,c}^e$ denote the centers of the boxes containing $\tilde{\boldsymbol{\rho}}_q^s$ and $\tilde{\boldsymbol{\rho}}_p^e$,

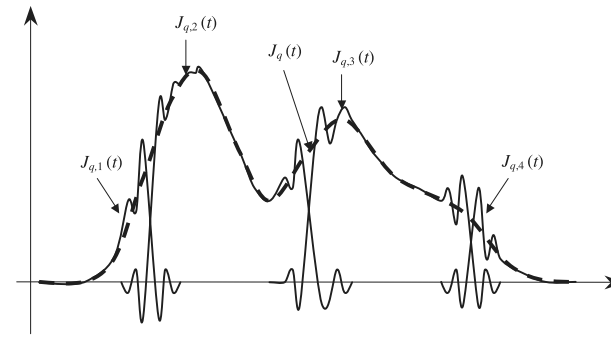

Figure 4. Split of a time domain signal.

and let $\mathbf{R}_{c,e} = \tilde{\boldsymbol{\rho}}_{p,c}^e - \tilde{\boldsymbol{\rho}}_{q,c}^s$, as shown in Figure 5. To simplify the description of the algorithm that follows, assume that $\tilde{\boldsymbol{\rho}}_q^s$ and $\tilde{\boldsymbol{\rho}}_p^h$ belong to a (possibly different) far-field-pair residing at the same level as that describing the $\tilde{\boldsymbol{\rho}}_q^s$ to $\tilde{\boldsymbol{\rho}}_p^e$ interaction; furthermore, let $\tilde{\boldsymbol{\rho}}_{p,c}^h$ denote the center of the box containing $\tilde{\boldsymbol{\rho}}_p^h$, let $\mathbf{R}_{c,h} = \tilde{\boldsymbol{\rho}}_{p,c}^h - \tilde{\boldsymbol{\rho}}_{q,c}^s$ and let $R_{c,e/h} = |\mathbf{R}_{c,e/h}|$.

[17] Next, pseudo-fields $\tilde{E}_{pq,v}(t)$ and $\tilde{H}_{pq,v}(t)$ are defined as

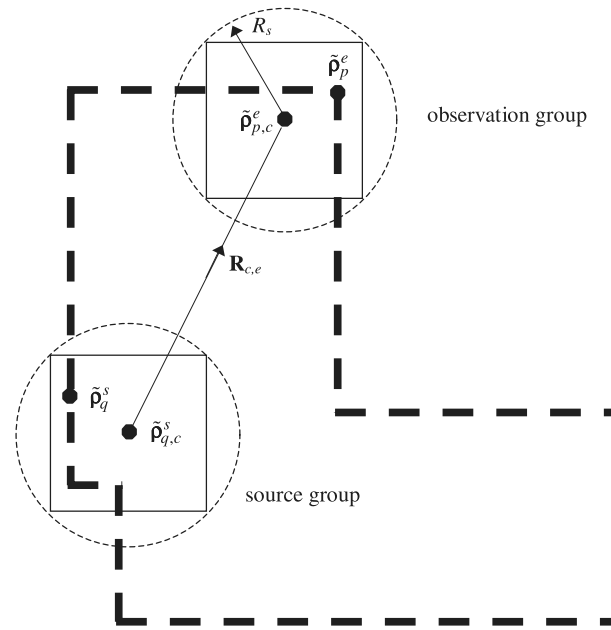

Figure 5. Illustration of the geometrical notations in PWTD algorithm.

$$\tilde{E}_{pq,v}(t) = \left[-\mu_0 w_q \partial_t \sum_{n=-N_\phi}^{N_\phi} \delta\left[t - \frac{\left(\boldsymbol{\rho} - \tilde{\boldsymbol{\rho}}^e_{p,c}\right)\cdot \hat{\mathbf{k}}(\phi_n)}{c} \right] \right. .$$
$$* \mathsf{H}\left\{ T_n\left(\tilde{\boldsymbol{\rho}}^e_{p,c} - \tilde{\boldsymbol{\rho}}^s_{q,c}, t\right) \right.$$
$$\left. * \delta\left[t - \frac{\left(\tilde{\boldsymbol{\rho}}^s_{q,c} - \tilde{\boldsymbol{\rho}}^s_{q}\right)\cdot \hat{\mathbf{k}}(\phi_n)}{c} \right] * J_{q,v}(t) \right\} \Bigg]_{\boldsymbol{\rho}=\tilde{\boldsymbol{\rho}}^e_p}$$
$$- \left[\hat{\mathbf{z}} \cdot \nabla \times w_q \hat{\mathbf{t}}^s\left(\tilde{\boldsymbol{\rho}}^s_q\right) \right.$$
$$\cdot \sum_{n=-N_\phi}^{N_\phi} \delta\left[t - \frac{\left(\boldsymbol{\rho} - \tilde{\boldsymbol{\rho}}^e_{p,c}\right)\cdot \hat{\mathbf{k}}(\phi_n)}{c} \right]$$
$$* \mathsf{H}\left\{ T_n\left(\tilde{\boldsymbol{\rho}}^e_{p,c} - \tilde{\boldsymbol{\rho}}^s_{q,c}, t\right) \right.$$
$$\left. * \delta\left[t - \frac{\left(\tilde{\boldsymbol{\rho}}^s_{q,c} - \tilde{\boldsymbol{\rho}}^s_{q}\right)\cdot \hat{\mathbf{k}}(\phi_n)}{c} \right] * K_{q,v}(t) \right\} \Bigg]_{\boldsymbol{\rho}=\tilde{\boldsymbol{\rho}}^e_p} \tag{21}$$

$$\tilde{H}_{pq,v}(t) = \left[w_q \hat{\mathbf{t}}^h(\boldsymbol{\rho}) \cdot \nabla \times \hat{\mathbf{z}} \sum_{n=-N_\phi}^{N_\phi} \delta\left[t - \frac{\left(\boldsymbol{\rho} - \tilde{\boldsymbol{\rho}}^h_{p,c}\right)\cdot \hat{\mathbf{k}}(\phi_n)}{c} \right] \right.$$
$$* \mathsf{H}\left\{ \mathsf{T}_n\left(\tilde{\boldsymbol{\rho}}^h_{p,c} - \tilde{\boldsymbol{\rho}}^s_{q,c}, t\right) \right.$$
$$\left. * \delta\left[t - \frac{\left(\tilde{\boldsymbol{\rho}}^s_{q,c} - \tilde{\boldsymbol{\rho}}^s_{q}\right)\cdot \hat{\mathbf{k}}(\phi_n)}{c} \right] * J_{q,v}(t) \right\} \Bigg]_{\boldsymbol{\rho}=\tilde{\boldsymbol{\rho}}^h_p}$$
$$- \left[w_q \hat{\mathbf{t}}^h(\boldsymbol{\rho}) \cdot \varepsilon_0 \int_{-\infty}^{t} dt' \left(\partial_{t'}^2 \bar{\mathbf{I}} - c^2 \nabla\nabla\right) \right.$$
$$\cdot \hat{\mathbf{t}}\left(\tilde{\boldsymbol{\rho}}^s_q\right) \sum_{n=-N_\phi}^{N_\phi} \delta\left[t' - \frac{\left(\boldsymbol{\rho} - \tilde{\boldsymbol{\rho}}^h_{p,c}\right)\cdot \hat{\mathbf{k}}(\phi_n)}{c} \right]$$
$$* \mathsf{H}\left\{ \mathsf{T}_n\left(\tilde{\boldsymbol{\rho}}^h_{p,c} - \tilde{\boldsymbol{\rho}}^s_{q,c}, t'\right) \right.$$
$$\left. * \delta\left[t' - \frac{\left(\tilde{\boldsymbol{\rho}}^s_{q,c} - \tilde{\boldsymbol{\rho}}^s_{q}\right)\cdot \hat{\mathbf{k}}(\phi_n)}{c} \right] * K_{q,v}(t') \right\} \Bigg]_{\boldsymbol{\rho}=\tilde{\boldsymbol{\rho}}^h_p}, \tag{22}$$

where H denotes a Hilbert transform, $N_\phi = \lceil \chi 2R_s\, \omega_{\max}/c \rceil$, "$\lceil\cdot\rceil$" stands for "the nearest larger integer," χ is an oversampling ratio, $\hat{\mathbf{k}}(\phi_n) = \hat{\mathbf{x}} \cos\phi_n + \hat{\mathbf{y}} \sin\phi_n$, $\phi_n = 2\pi n/(2N_\phi + 1)$,

$$\mathsf{T}_n(\boldsymbol{\rho}, t) = \frac{1}{2\pi\left(2N_\phi + 1\right)} \frac{c}{|\boldsymbol{\rho}|} \sum_{m=0}^{N_\phi} \varepsilon_m \cos[m(-\phi_n + \angle\boldsymbol{\rho})]$$
$$\cdot \frac{T_m(ct/|\boldsymbol{\rho}|)}{\sqrt{1 - (ct/|\boldsymbol{\rho}|)^2}} P\left(t, \frac{|\boldsymbol{\rho}|}{c}\right), \tag{23}$$

T_m is the Chebyshev polynomial of degree m, $\angle\boldsymbol{\rho}$ is the angle between $\hat{\mathbf{x}}$ and $\boldsymbol{\rho}$, $\varepsilon_m = 1$ for $m = 0$; $\varepsilon_m = 2$ for $m \neq 0$ (Neumann number), and pulse function $P(\cdot,\cdot)$ is defined as

$$P(x, y) = \begin{cases} 1 & |x| \leq y \\ 0 & |x| > y \end{cases}. \tag{24}$$

It is apparent that the outer sum over n in equations (21) and (22) arises from a discrete evaluation of a spectral integral, and that the pseudo-fields comprise a summation of $2N_\phi + 1$ "plane waves" traveling in directions $\hat{\mathbf{k}}(\phi_n)$, $n = -N_\phi, -N_{\phi+1}, \ldots N_\phi$.

[18] The above expressions in equations (21) and (22) are straightforward generalizations of the pseudo-scalar field representation of *Lu et al.* [2000, equation (31)]. In other words, these expressions are arrived at by mechanically applying the plane wave decomposition of *Lu et al.* [2000] to each of the four terms in equations (19) and (20) involving a convolution with $g(\rho, t)$. It then follows from *Lu et al.* [2000] that, as long as the temporal duration of $J_{q,v}(t)$ and $K_{q,v}(t)$ is less than $(R_{c,e/h} - 2R_s)/c$, the ghost signal can be time-gated so that $\tilde{E}_{pq,v}(t)$ and $\tilde{H}_{pq,v}(t)$ equal $E_{pq,v}(t)$ and $H_{pq,v}(t)$, respectively, to within an error that can be made arbitrarily small (by increasing oversampling ratios, with superalgebraic convergence). By using standard vector identities and the fact that $\nabla \Longleftrightarrow -\partial_t \hat{\mathbf{k}}(\phi_n)/c$ for plane waves traveling in the direction $\hat{\mathbf{k}}(\phi_n)$, equations (21) and (22) can be further simplified to

$$\tilde{E}_{pq,v}(t) = -\int_0^t dt' \sum_{n=-N_\phi}^{N_\phi} \delta\left[t' - \frac{\left(\tilde{\boldsymbol{\rho}}^e_p - \tilde{\boldsymbol{\rho}}^e_{p,c}\right)\cdot \hat{\mathbf{k}}(\phi_n)}{c} \right]$$
$$*_{(4)} \mathsf{H}_{(3)} \left\{ \frac{\partial^2}{\partial t'^2} \mathsf{T}_n\left(\tilde{\boldsymbol{\rho}}^e_{p,c} - \tilde{\boldsymbol{\rho}}^s_{q,c}, t'\right) \cdot \right.$$
$$*_{(2)} \delta\left[t' - \frac{\left(\tilde{\boldsymbol{\rho}}^s_{q,c} - \tilde{\boldsymbol{\rho}}^s_{q}\right)\cdot \hat{\mathbf{k}}(\phi_n)}{c} \right]$$
$$*_{(1)} w_q \left[\mu_0 J_{q,v}(t') - \frac{1}{c} \hat{\mathbf{n}}^s\left(\tilde{\boldsymbol{\rho}}^s_q\right) \right.$$
$$\left. \left. \cdot \hat{\mathbf{k}}(\phi_n) K_{q,v}(t') \right] \right\} \tag{25}$$

$$\tilde{H}_{pq,v}(t) = -\int_0^t dt' \sum_{n=-N_\phi}^{N_\phi} \left\{ \frac{1}{\eta_0} \hat{\mathbf{t}}^h\left(\tilde{\boldsymbol{\rho}}_p^h\right) \cdot \hat{\mathbf{k}}(\phi_n) \times \hat{\mathbf{z}} \right\} \cdot \delta\left[t' - \frac{\left(\tilde{\boldsymbol{\rho}}_p^h - \tilde{\boldsymbol{\rho}}_{p,c}^h\right) \cdot \hat{\mathbf{k}}(\phi_n)}{c} \right] * {}_{(4)}\mathsf{H}_{(3)} \left\{ \frac{\partial^2}{\partial t'^2} \mathsf{T}_n\left(\tilde{\boldsymbol{\rho}}_{p,c}^h - \tilde{\boldsymbol{\rho}}_{q,c}^s, t'\right) . * {}_{(2)}\delta\left[t' - \frac{\left(\tilde{\boldsymbol{\rho}}_{q,c}^s - \tilde{\boldsymbol{\rho}}_q^s\right) \cdot \hat{\mathbf{k}}(\phi_n)}{c} \right] * {}_{(1)} w_q \left[\mu_0 J_{q,v}(t') - \frac{1}{c} \hat{\mathbf{n}}^s\left(\tilde{\boldsymbol{\rho}}_q^s\right) \cdot \hat{\mathbf{k}}(\phi_n) K_{q,v}(t') \right] \right\}, \quad (26)$$

where $\eta_0 = \sqrt{\mu_0/\varepsilon_0}$ is the wave impedance in the free space. Equations (25) and (26) form the crux of the proposed fast TBC kernel and are used to compute fields $\tilde{E}_{pq,v}(t)$ and $\tilde{H}_{pq,v}(t)$ using a scheme comprising four steps that implement the subscripted temporal convolutions/Hilbert transforms in equations (25) and (26). These four steps are described in more detail below.

[19] (1) The source signals $J_{q,v}(t)$ and $K_{q,v}(t)$ are projected from the source point(s) $\tilde{\boldsymbol{\rho}}_q^s$ onto plane waves traveling in the directions $\hat{\mathbf{k}}(\phi_n)$, $n = -N_\phi, -N_{\phi+1}, \ldots N_\phi$ (Figure 6a):

$$\delta\left[t' - \frac{\left(\boldsymbol{\rho} - \tilde{\boldsymbol{\rho}}_q^s\right) \cdot \hat{\mathbf{k}}(\phi_n)}{c} \right] * w_q \left[\mu_0 J_{q,v}(t') - \frac{1}{c} \hat{\mathbf{n}}^s\left(\tilde{\boldsymbol{\rho}}_q^s\right) \cdot \hat{\mathbf{k}}(\phi_n) K_{q,v}(t') \right]. \quad (27)$$

When the $2N_\phi + 1$ plane waves are observed at the center of the source box center $\tilde{\boldsymbol{\rho}}_{q,c}^s$, the resulting signals are termed outgoing rays:

$$\mathsf{O}(\phi_n, t') = \delta\left[t' - \frac{\left(\tilde{\boldsymbol{\rho}}_{q,c}^s - \tilde{\boldsymbol{\rho}}_q^s\right) \cdot \hat{\mathbf{k}}(\phi_n)}{c} \right] * w_q \left[\mu_0 J_{q,v}(t') - \frac{1}{c} \hat{\mathbf{n}}^s\left(\tilde{\boldsymbol{\rho}}_q^s\right) \cdot \hat{\mathbf{k}}(\phi_n) K_{q,v}(t') \right]. \quad (28)$$

[20] (2) The outgoing rays are translated onto plane waves traveling in the directions $\hat{\mathbf{k}}(\phi_n)$, $n = -N_\phi, -N_{\phi+1}, \ldots N_\phi$ as (Figure 6b):

$$\delta\left[t' - \frac{\left(\boldsymbol{\rho} - \tilde{\boldsymbol{\rho}}_{p,c}^{e/h}\right) \cdot \hat{\mathbf{k}}(\phi_n)}{c} \right] * \left[\frac{\partial^2}{\partial t'^2} \mathsf{T}_n\left(\tilde{\boldsymbol{\rho}}_{p,c}^{e/h} - \tilde{\boldsymbol{\rho}}_{q,c}^s, t'\right) * \mathsf{O}(\phi_n, t') \right]. \quad (29)$$

The time signatures of the resulted plane waves when observed at the observation box centers $\tilde{\boldsymbol{\rho}}_{p,c}^{e/h}$ are termed incoming rays:

$$\mathsf{I}(\phi_n, t') = \frac{\partial^2}{\partial t'^2} \mathsf{T}_n\left(\tilde{\boldsymbol{\rho}}_{p,c}^{e/h} - \tilde{\boldsymbol{\rho}}_{q,c}^s, t'\right) * \mathsf{O}(\phi_n, t'). \quad (30)$$

[21] (3) All incoming rays are Hilbert transformed. It is noted that Hilbert transformed incoming rays become infinitely long in time, although the incoming rays have finite temporal durations (Figure 6c). The multiresolution scheme described in the work of *Lu et al.* [2000] is used to efficiently accomplish/represent the Hilbert transformed incoming rays.

[22] (4) The Hilbert transformed incoming rays are projected onto the observation points $\tilde{\boldsymbol{\rho}}_p^{e/h}$ as (Figure 6d):

$$\delta\left[t' - \frac{\left(\tilde{\boldsymbol{\rho}}_p^{e/h} - \tilde{\boldsymbol{\rho}}_{p,c}^{e/h}\right) \cdot \hat{\mathbf{k}}(\phi_n)}{c} \right] * \mathsf{H}\{\mathsf{I}(\phi_n, t')\}. \quad (31)$$

The pseudo-fields $\tilde{E}_{pq,v}(t)$ or $\tilde{H}_{pq,v}(t)$ are obtained by summing up projections of Hilbert transformed incoming rays from all of the $2N_\phi + 1$ directions. As shown in Figure 6d, the pseudo-fields always contain true and ghost contributions. These contributions however are temporally isolated if the temporal duration of the subsignals ($J_{q,v}(t)$ and $K_{q,v}(t)$) satisfy the requirement described in the above. As a result, the ghost signals can be easily removed and true fields recorded.

[23] The key differences between equations (25) and (26) and the corresponding scalar field expressions in the work of *Lu et al.* [2000] are summarized below:

[24] (1) A direction-dependent factor $\hat{\mathbf{n}}^s(\tilde{\boldsymbol{\rho}}_q^s) \cdot \hat{\mathbf{k}}(\phi_n)$ needs to be considered when the source signal $K_{q,v}(t')$ at $\tilde{\boldsymbol{\rho}}_q^s$ is projected to the outgoing ray traveling in direction $\hat{\mathbf{k}}(\phi_n)$.

[25] (2) An additional double time derivative is to be accounted for in the translation function. Because, in practice, translation operation is most efficiently computed in the spectral domain, inclusion of time derivatives in the translation operation poses no problems.

[26] (3) The projection from plane waves to the actual observers differs for electric and magnetic fields. Electric fields are obtained through a simple summation of the plane waves from all the directions, while additional

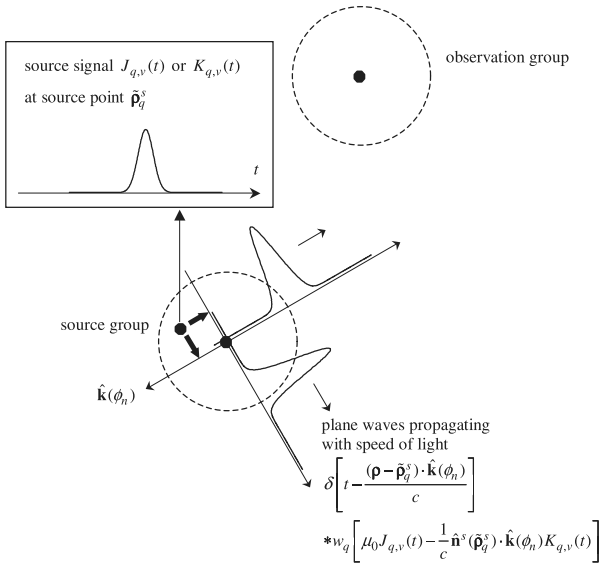

(a) projection from source points to outgoing rays

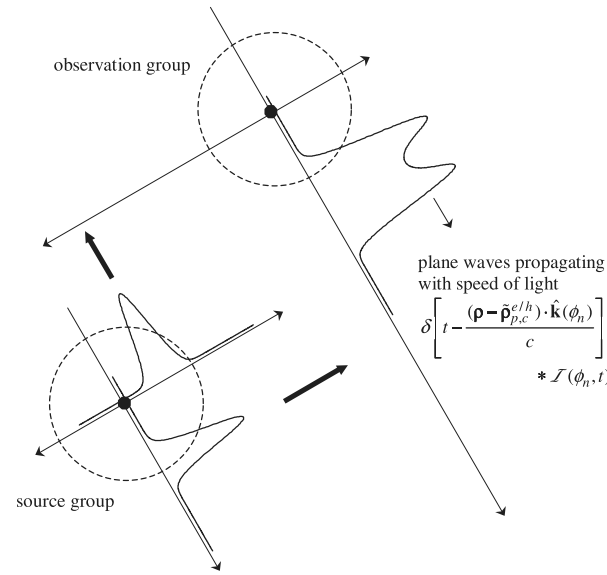

(b) translation from outgoing rays to incoming rays

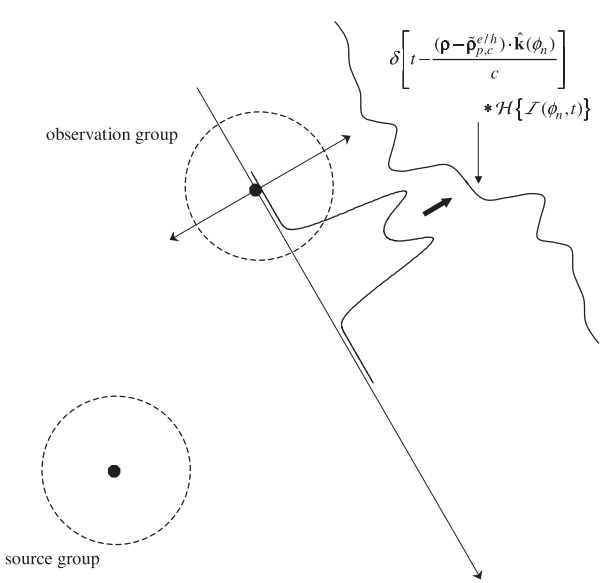

(c) Hilbert transformation on the incoming rays

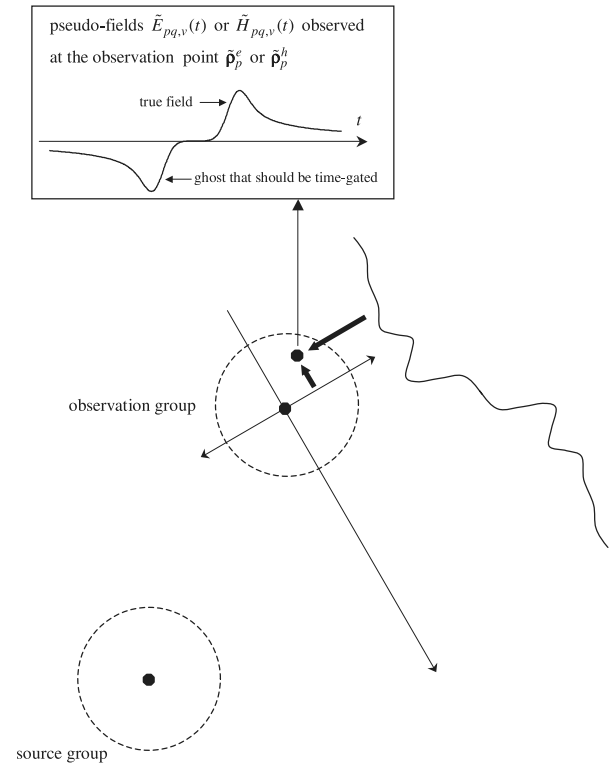

(d) projection from the Hilbert transformed incoming rays to the observation points

Figure 6

direction-dependent factors $\hat{\mathbf{t}}^h(\tilde{\boldsymbol{\rho}}_p^h) \cdot \hat{\mathbf{k}}(\phi_n) \times \hat{\mathbf{z}}/\eta_0$ are needed when adding up the contributions from all the plane waves for magnetic fields.

[27] (4) The summed up plane waves are to be integrated w.r.t. time. Note that the time integral and time derivatives should not be cancelled as it will induce an undesirable static ghost signal.

[28] (5) In the work of *Lu et al.* [2000], it is assumed that the number of discrete sources is the same as that of discrete observers, and the sources and observers coincide spatially. Here, this is not the case. However as long as the source and the observation boundaries reside close to each other, $\tilde{N}^s \approx \tilde{N}^h \approx \tilde{N}^e$ as was assumed above, and the three surfaces form one thick interface, the width of which does not grow with the problem size.

[29] It is easily verified that the above five revisions do not affect the computational complexity analysis reported in the work of *Lu et al.* [2000]. Therefore the computational complexity of the PWTD-accelerated combined field global TBC for 2-D FDTD is $O(\tilde{N}^s \tilde{N}^t \log \tilde{N}^s \log \tilde{N}^t)$, as opposed to $O(\tilde{N}^{s^2} \tilde{N}^{t^2})$ for a classical kernel. The reader is referred to *Lu et al.* [2000] for a detailed derivation of the scheme's computational complexity. The key mechanisms leading to a reduction in computational complexity however are clear from the above described four-step process. Time-acceleration, viz. the reduction in temporal complexity from $O(\tilde{N}^{t^2})$ to $O(\tilde{N}^t \log \tilde{N}^t)$ is due to the realization that the time domain Green function tail can be represented using a Hilbert transform. Indeed, this realization leads to efficient multiresolution representations of and temporal convolution schemes for fields produced by 2-D source constellations. Space-acceleration, viz. the reduction in spatial complexity from $O(\tilde{N}^{s^2})$ to $O(\tilde{N}^s \log \tilde{N}^s)$, is due to the plane wave decomposition of the time domain Green function, which permits the "diagonal translation" of fields, much like in frequency domain/Helmholtz equation fast multipole schemes [*Coifman et al.*, 1993; *Song et al.*, 1997].

[30] Because the numerical error introduced by the PWTD algorithm can be made arbitrarily small as shown in the work of *Lu et al.* [2000], the evaluation of the combined field global TBC kernel can be accelerated by the PWTD algorithm without loss of accuracy.

[31] The above discussion focused on far-field interactions. Interactions between points in near-field boxes are accounted for by treating each pair of points separately. The required temporal convolutions can be accelerated in many ways: (1) using the fast Fourier transform (FFT) method of *Hairer et al.* [1985], (2) using an extension of the scheme that relies on truncated singular value decompositions [*Lu et al.*, 2004b], and (3) using the PWTD scheme in the limit $R_s \to 0$ [*Lu et al.*, 2000, 2004b]. The implementation and performance of these three accelerators are studied in detail in the work of *Lu et al.* [2004b]. None of them increases the computational complexity of the method above that of the far-field component.

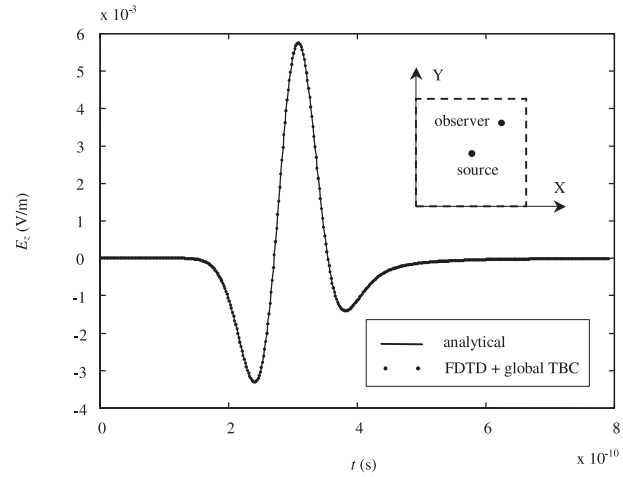

Figure 7. Numerical results for the radiation of a line source in free space.

3. Numerical Results

[32] In this section, numerical experiments are described that validate and test the efficiency of the proposed PWTD-enhanced global TBC scheme. In the first example, the field due to a line source $J_z^e(\boldsymbol{\rho}, t) = \delta(\boldsymbol{\rho} - (\hat{\mathbf{x}}\ 12.5\ \text{mm} + \hat{\mathbf{y}}\ 12.5\ \text{mm}))f(t)$ radiating in free space is computed. The temporal signature of the source is modeled by a Neumann pulse, viz.,

$$f(t) = -\frac{t - t_0}{\sigma} e^{\frac{-(t-t_0)^2}{2\sigma^2}}, \tag{32}$$

with $\sigma = 3.716 \times 10^{-11}$ s and $t_0 = 2.6 \times 10^{-10}$ s. The source resides in the center of the FDTD computational domain that is anchored at the origin and modeled in terms of 25×25 cells with $\Delta x = \Delta y = 1$ mm; the time step is $\Delta t = 1.688 \times 10^{-12}$ s. A combined field TBC with $\alpha = 0.5$ is used to truncate the computational domain. The electric field at $\hat{\mathbf{x}}19.5 + \hat{\mathbf{y}}19.5$ mm is plotted

Figure 6. Four-step implementation of the PWTD algorithm. (a) Projection from source points to outgoing rays. (b) Translation from outgoing rays to incoming rays. (c) Hilbert transformation on the incoming rays. (d) Projection from the Hilbert transformed incoming rays to the observation points.

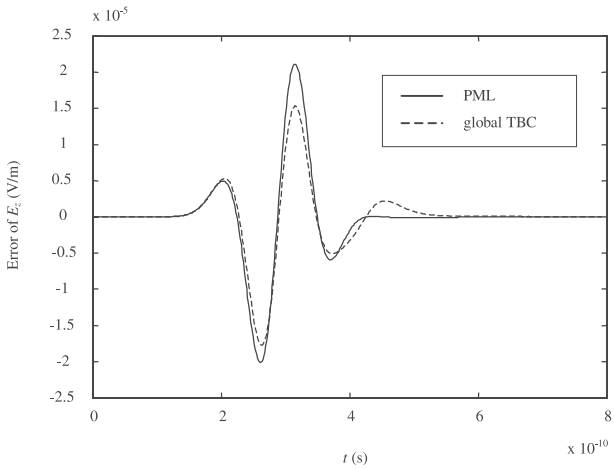

Figure 8. Accuracy comparison between global TBC and PML.

in Figure 7. The numerical solution visually agrees with the exact one. The difference between them is plotted in Figure 8. Similar data is plotted for a numerical solution obtained using a 13 layer perfectly matched boundary placed outside the aforementioned FDTD domain. It is observed that in terms of accuracy the global TBC performs as well as the PML.

[33] Scattering by a square object with relative permittivity $\varepsilon_r = 4.0$ under plane wave incidence is analyzed next. The incident electric field is

$$E_z^i(\boldsymbol{\rho}, t) = -\frac{t - t_0 - \boldsymbol{\rho} \cdot \hat{\mathbf{k}}^i / c}{\sigma} e^{\frac{-(t - t_0 - \boldsymbol{\rho} \cdot \hat{\mathbf{k}}^i / c)^2}{2\sigma^2}}, \qquad (33)$$

where $\sigma = 3.716 \times 10^{-11}$ s, $t_0 = 2.6 \times 10^{-10}$, $\hat{\mathbf{k}}^i = \cos \phi^i \hat{\mathbf{x}} + \sin \phi^i \hat{\mathbf{y}}$ and $\phi^i = 45°$. There are 71×71 cells in the FDTD domain, which is anchored at the origin and has $\Delta x = \Delta y = 1$ mm with $\Delta t = 1.668 \times 10^{-12}$ s. The square scatterer occupies 41×41 cells and is put in the center of the FDTD domain. The electric field at $\hat{\mathbf{x}}35.5 + \hat{\mathbf{y}}35.5$ mm is plotted in Figure 9. The results obtained using a PML and combined field TBC ($\alpha = 0.6$) agree very well.

[34] Scattering from an L-shaped dielectric strip with $\varepsilon_r = 4.0$ is simulated next; this example also serves to demonstrate the computational complexity of the scheme. Each arm of the strip covers 50×2 cells. The tip of the L resides at $\hat{\mathbf{x}}9 + \hat{\mathbf{y}}9$ mm. The incident field and all other parameters remain unchanged from the previous example. The electric field at $\hat{\mathbf{x}}9.5 + \hat{\mathbf{y}}9.5$ mm is plotted in Figure 10. The results obtained using the PML and the combined field TBC kernels are in excellent agreement. This specific example is intended to show the advantage of the global TBC kernel over the PML for thin, concave scatterers. Suppose that one arm of the strip scatterer has length l, that its width w is much less than l, and that $\Delta x = \Delta y = \Delta s$. In what follows, l is scaled while w is kept fixed. To analyze this scattering problem using a PML truncated FDTD mesh, the scatterer has to be enclosed in a large square box with side-length approximately equal to l (Figure 11a). The relative numerical error in the phase velocity associated with the Yee FDTD scheme scales as $(\Delta s/\lambda_{\min})^2$ [*Chew*, 1995]. The accumulated phase dispersion error over the FDTD domain therefore is proportional to $(\Delta s/\lambda_{\min})^2 (l/\lambda_{\min})$. To control the overall dispersion error, Δs should be reduced when l is increased. At the same time, the time step size has to be reduced accordingly to satisfy the CFL stability criterion of the Yee FDTD scheme. In the numerical example that follows, Δs and Δt are reduced to limit the dispersion error associated with one traversal of the computational domain to 10 degrees. Therefore, when the FDTD domain is

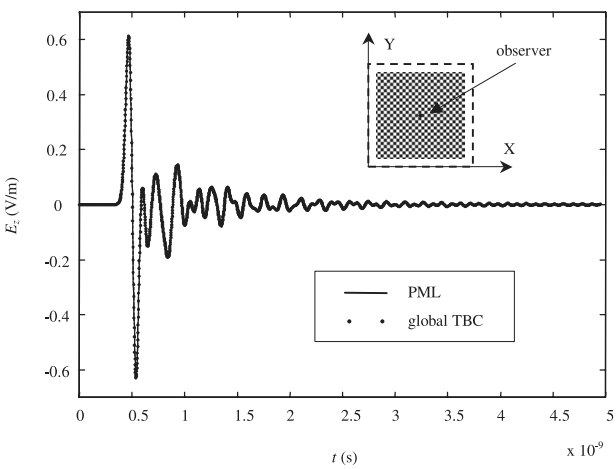

Figure 9. Numerical results for the scattering from a square scatterer.

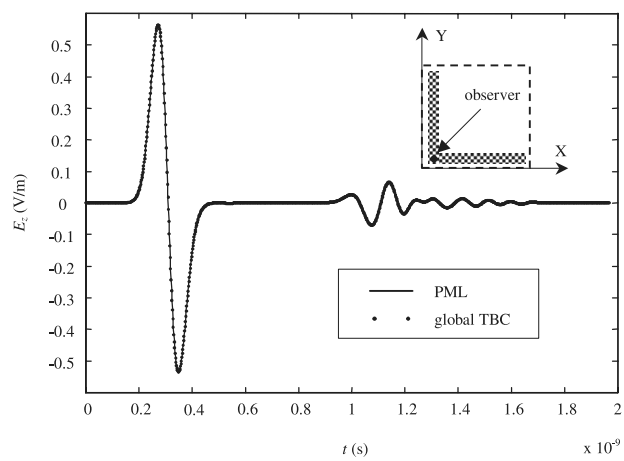

Figure 10. Numerical results for the scattering from a bent strip.

Table 1. Comparison Between the Computational Costs of PWTD-Accelerated Global TBC and PML[a]

	Cost for Bulk FDTD Update	Cost for BC Update
PWTD-accelerated global TBC	$O(L^3)/O(L^2)$	$O(L^2 \log^2 L)/O(L^2 \log^2 L)$
Classically evaluated global TBC	$O(L^3)/O(L^2)$	$O(L^4)/O(L^4)$
PML	$O(L^{4.5})/O(L^3)$	$O(L^3)/O(L^2)$

[a]The left entry in each table cell refers to costs associated with a YEE FDTD scheme, while the right entry gives a cost estimate for a higher-order solver without dispersion.

truncated by PML, the number of FDTD cells is proportional to $L^{1.5} \times L^{1.5}$ while the number of FDTD time steps grows as proportional to $L^{1.5}$, where $L = l/\lambda_{\min}$. In contrast, when the FDTD domain is truncated by a global TBC placed close to the L-shaped strip, the number of cells in the FDTD domain only scales as $O(L^{1.5})$ (Figure 11b). As mentioned before, the spatial discretization and time step size used when enforcing the global TBC are determined solely by $\lambda_{\min}$; therefore, provided that $T \propto l/c$ (a good assumption for nonresonant scatterers), $\tilde{N}^s \propto \tilde{N}^t \propto L$. The computational costs associated with the (bulk) FDTD updates and the evaluation of the boundary kernel are provided in Table 1 for Yee FDTD schemes truncated by PWTD-accelerated TBC kernels, classical TBC kernels, and PML kernels; dominant costs appear boxed. Also shown in this table are cost estimates for higher-order FDTD solvers in which grid dispersion would never be an issue, no matter how large the computational domain is. Irrespective of whether dispersion enters the picture or not, PWTD-accelerated global TBC kernels outperform PML kernels when applied to very large L-shaped geometries (or, in general, thin and concave structures). CPU times for a Yee FDTD with PML and PWTD-enhanced global TBC truncation for the L-shaped strip scatterer are shown in Figure 12. It is observed that the global PWTD-accelerated TBC scheme is faster than the PML when the scatterer is large enough. The crossover point is around $L = 35\lambda_{\min}$; i.e., when $L < 35\lambda_{\min}$, it is advantageous to use the PML and model field propagation between the legs of the L by propagating through the FDTD grid. However, when $L > 35\lambda_{\min}$, it becomes advantageous to replace the PML by a PWTD-accelerated TBC kernel. While this crossover size may seem large, it should come as no surprise. Fast-multipole kernels, and especially PWTD ones, typically outperform classical evaluation schemes when the number of spatial points is in the range 1000–2000, and a $|C^r| = 2 \times 50\lambda_{\min} = 100\lambda_{\min}$ sampled at 20 points per $\lambda_{\min}$ contains approximately 2000 points.

[35] Finally, to demonstrate the applicability of the proposed method to practical problems, a 2-D optical slab waveguide is analyzed. The waveguide structure is illustrated in Figure 13. The figure is for illustration purposes only as aspect ratios of the various components of this device were not maintained. The waveguide consists of dielectric material with $\varepsilon_r = 8.9$, and is surrounded by air. An electric line source with temporal signature

$$f(t) = e^{-\frac{(t-t_c)^2}{2\sigma^2}} \cos(\omega_0 t), \tag{34}$$

with $\sigma = 8.85 \times 10^{-15}$ s, $\omega_0 = 2\pi \times 18 \times 10^{13}$ rad/s, and $t_c = 8.85 \times 10^{-14}$ s is placed near the leftmost end of the waveguide, and excites the system. The spectrum of the excitation can be considered negligible beyond the frequency 360 THz. When the frequency is less than 360 THz, only the basic mode propagates in the

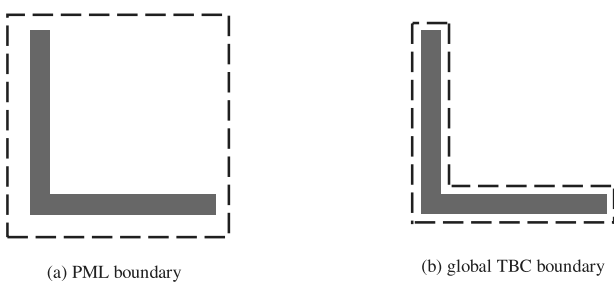

Figure 11. Illustration of the PML and global TBC for the bent strip.

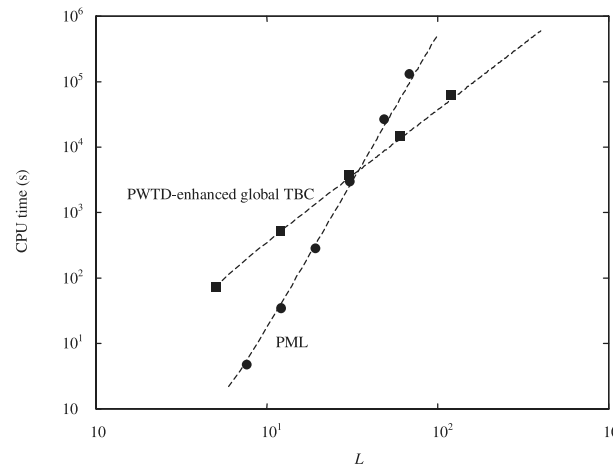

Figure 12. Computational complexity comparison between PWTD-accelerated global TBC and PML for the scattering from a bent strip.

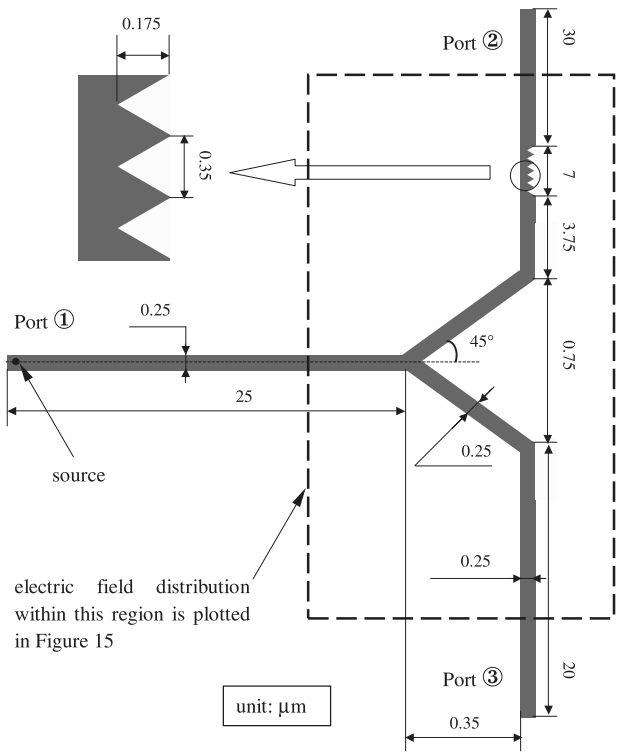

Figure 13. Illustration of the slab waveguide structure.

waveguide. When the wave travels to the junction, each of the two vertical arms absorbs half its energy. The junction is designed carefully so that reflections and spurious radiation at the junction are minimized. To complicate the problem, a band-stop filter is placed in the upper vertical arm. The filter contains 20 triangular corrugations. This problem was analyzed using both

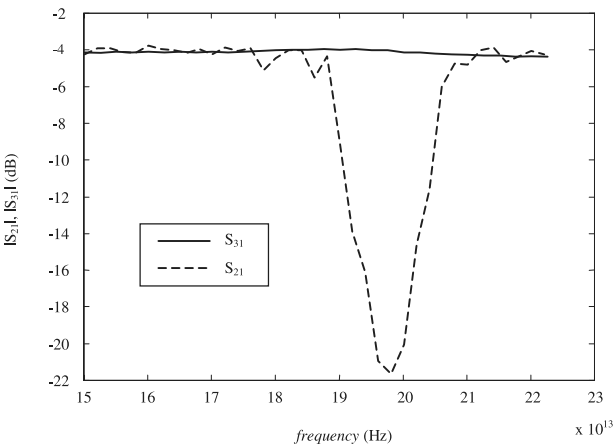

Figure 14. $|S_{31}|$ and $|S_{21}|$ of the slab waveguide.

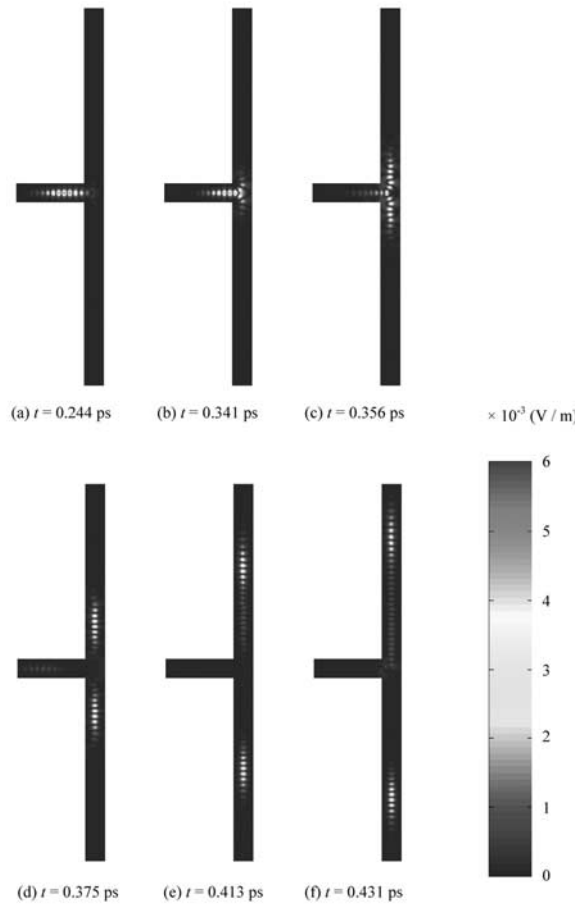

Figure 15. $|E_z|$ distributions within a portion of the waveguide at six temporal points. See color version of this figure at back of this issue.

PML and PWTD-based boundary kernels; for the latter, the truncation boundary was placed very close to the waveguide along its length. Only numerical results obtained using the PWTD code are shown; they always were in excellent agreement with those from the PML code. The S-parameters in the frequency range [150 THz, 230 THz] is computed and plotted in Figure 14 using the port definitions illustrated in Figure 13. It is observed that $|S_{31}|$ has values around -4.1 dB within this frequency range, and is almost independent of frequency. At the same time, a certain frequency band is filtered out by the corrugations in the upper arm, as evidenced by the $|S_{21}|$ plot. The electric field distribution within a portion of the structure is plotted in Figure 15 at the following time points: (a) t = 0.244 ps; (b) t = 0.341 ps; (c) t = 0.356 ps; (d) t = 0.375 ps; (e) t = 0.413 ps; and (f) t = 0.431 ps. The

wave's behavior when passing the junction and filter is clearly shown.

4. Conclusions

[36] In this study, the 2-D PWTD algorithm was used to impose a global TBC for 2-D FDTD solvers. The computational complexity of classical schemes for enforcing such TBCs scales as $O(\tilde{N}^{s^2}\tilde{N}^{t^2})$ but was reduced to $O(\tilde{N}^s\tilde{N}^t \log \tilde{N}^s \log \tilde{N}^t)$ by using the PWTD scheme. Numerical results show that this technique is both accurate and efficient. For large, thin, and concave scatterers, the scheme outperforms the PML.

[37] **Acknowledgment.** This work was supported in part by a grant from DARPA VET program under contract F49620-01-1-0228, ARO program under contract DAAD 19-00-1-0464, MURI grant F49620-01-1-04 "Analysis and design of ultra-wide band and high power microwave pulse interactions with electronic circuits and systems," and NSF under CCR: 9988347 and 0306436.

References

Alpert, B., L. Greengard, and T. Hagstrom (2000), Rapid evaluation of nonreflecting boundary kernels for time-domain wave propagation, *SIAM J. Numer. Anal.*, *37*(4), 1138–1164.

Berenger, J. P. (1994), A perfectly matched layer for the absorption of electromagnetic waves, *J. Comput. Phys.*, *114*, 185–200.

Bernardi, P., M. Cavagnaro, P. D'Atanasio, E. Di Palma, S. Pisa, and E. Piuzzi (2002), FDTD, multiple-region/FDTD, ray-tracing/FDTD: A comparison on their applicability for human exposure evaluation, *Int. J. Numer. Modell. Electron. Netw. Devices Fields*, *15*(5–6), 579–593.

Chew, W. C. (1995), *Waves and Fields in Inhomogeneous Media*, IEEE Press, New York.

Chew, W. C., and W. H. Weedon (1994), A 3D perfectly matched medium from modified Maxwell's equations with stretched coordinates, *Microw. Opt. Technol. Lett.*, *7*(13), 599–604.

Chew, W. C., J. M. Jin, and E. Michielssen (1997), Complex coordinate stretching as a generalized absorbing boundary condition, *Microw. Opt. Technol. Lett.*, *15*(6), 363–369.

Coifman, R., V. Rokhlin, and S. Wandzura (1993), The fast multipole method for the wave equation: A pedestrian prescription, *IEEE Antennas Propagat. Mag.*, *35*(3), 7–12.

De Moerloose, J., and D. De Zutter (1993), Surface integral representation radiation boundary condition for the FDTD method, *IEEE Trans. Antennas Propag.*, *41*(7), 890–896.

Djordjevic, A. R., T. K. Sarkar, and T. Roy (1995), Finite-difference solution of scattering (TE case) using exact mesh termination, *Microw. Opt. Technol. Lett.*, *10*(1), 56–59.

Engquist, B., and A. Majda (1977), Absorbing boundary conditions for the numerical simulation of waves, *Math. Comput.*, *31*(139), 629–651.

Givoli, D., and D. Cohen (1995), Nonreflecting boundary conditions based on Kirchhoff-type formulae, *J. Comput. Phys.*, *117*(1), 102–113.

Grote, M. J., and J. B. Keller (1998), Nonreflecting boundary conditions for Maxwell's equations, *J. Comput. Phys.*, *139*(2), 327–342.

Grote, M. J., and J. B. Keller (2000), Exact nonreflecting boundary condition for elastic waves, *SIAM J. Appl. Math.*, *60*, 803–819.

Hairer, E., C. Lubich, and M. Schlichte (1985), Fast numerical solution of nonlinear Volterra convolution equations, *SIAM J. Sci. Statist. Comput.*, *6*(3), 532–541.

Higdon, R. L. (1987), Numerical absorbing boundary conditions for the wave equation, *Math. Comput.*, *49*(179), 65–90.

Holtzman, R., and R. Kastner (2001), The time-domain discrete Green's function method (GFM) characterizing the FDTD grid boundary, *IEEE Trans. Antennas Propag.*, *49*, 1079–1093.

Johnson, J. M., and Y. Rahmat-Samii (1997), MR/FDTD: A multiple-region finite-difference-time-domain method, *Microw. Opt. Technol. Lett.*, *14*(2), 101–105.

Keller, J. B., and D. Givoli (1989), Exact non-reflecting boundary conditions, *J. Comput. Phys.*, *82*(1989), 172–192.

Liao, Z. P., H. L. Wong, B. P. Yang, and Y. F. Yuan (1984), A transmitting boundary for transient wave analyses, *Sci. Sinica, Ser. A*, *XXVII*, 1063–1076.

Lu, M., J. Wang, A. A. Ergin, and E. Michielssen (2000), Fast evaluation of two-dimensional transient wave fields, *J. Comput. Phys.*, *158*(2), 161–185.

Lu, M., B. Shanker, and E. Michielssen (2004a), Elimination of spurious solutions associated with exact transparent boundary conditions in FDTD solvers, *IEEE Antennas Wireless Propagat. Lett.*, *3*, 59–62.

Lu, M., K. Yegin, B. Shanker, and E. Michielssen (2004b), Fast time domain integral equation solvers for analyzing two-dimensional scattering phenomena: Part I. Temporal acceleration, *Electromagnetics*, in press.

Lubich, C., and A. Schadle (2002), Fast convolution for non-reflecting boundary conditions, *SIAM J. Sci. Comput.*, *24*(1), 161–182.

Mur, G. (1981), Absorbing boundary conditions for the finite-difference approximation of the time-domain electromagnetic-field equations, *IEEE Trans. Electromagn. Compat.*, *23*(4), 377–382.

Oliver, J. C. (1992), On the synthesis of exact free space absorbing boundary conditions for the finite-difference-time-domain method, *IEEE Trans. Antennas Propag.*, *40*(4), 456–460.

Song, J. M., C. C. Lu, and W. C. Chew (1997), MLFMA for electromagnetic scattering by large complex objects, *IEEE Trans. Antennas Propag.*, *45*, 1488–1493.

Taflove, A. (1995), *Computational Electrodynamics: The Finite-Difference Time-Domain Method*, Artech House, Norwood, Mass.

Ting, L., and M. J. Miksis (1986), Exact boundary conditions for scattering problems, *J. Acoust. Soc. Am.*, *80*(6), 1825–1827.

Wu, X., and O. M. Ramahi (2002), Application of the concurrent complementary operators method to numerically derived absorbing boundary conditions, *Microw. Opt. Technol. Lett.*, *32*(4), 272–275.

Yee, K. S. (1966), Numerical solution of initial boundary value problems involving Maxwell's equations in isotropic media, *IEEE Trans. Antennas Propag.*, *14*, 302–307.

Ziolkowski, R. W., N. K. Madsen, and R. C. Carpenter (1983), Three-dimensional computer modeling of electromagnetic fields: A global lookback lattice truncation scheme, *J. Comput. Phys.*, *50*, 360–408.

A. A. Ergin, M. Lu, M. Lv, and E. Michielssen, Center for Computational Electromagnetics, Department of Electrical and Computer Engineering, University of Illinois at Urbana-Champaign, Urbana, IL 61801, USA. (mlu@emlab.uiuc.edu)

B. Shanker, Electromagnetics Research Group, Department of Electrical and Computer Engineering, Michigan State University, 2120 Engineering Building, East Lansing, MI 48824, USA.

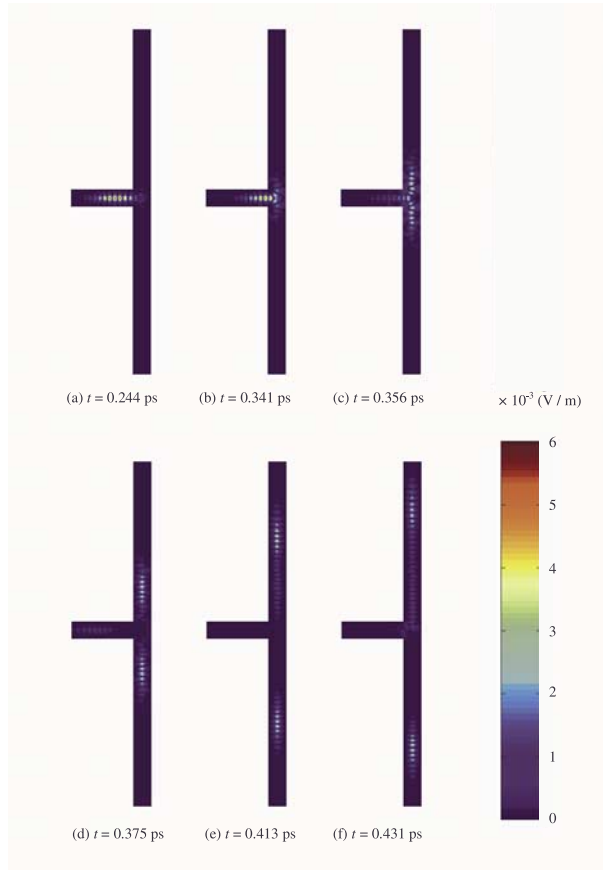

Figure 15. $|E_z|$ distributions within a portion of the waveguide at six temporal points.